# Anisotropy and Coherent Vortex Structures in Planetary Turbulence

James C. McWilliams, Jeffrey B. Weiss, Irad Yavneh

**High-resolution numerical simulations were made of unforced, planetary-scale fluid dynamics. In particular, the simulation was based on the quasi-geostrophic equations for a Boussinesq fluid in a uniformly rotating and stably stratified environment, which is an idealization for large regions of either the atmosphere or ocean. The solutions show significant discrepancies from the long-standing theoretical prediction of isotropy. The discrepancies are associated with the self-organization of the flow into a large population of coherent vortices. Their chaotic interactions govern the subsequent evolution of the flow toward a final configuration that is nonturbulent.**

Fluid motions in planetary atmospheres and oceans are often strongly influenced by planetary rotation and stable vertical density stratification. These flows exhibit a rich phenomenology of global-scale circulations and long-lived vortices. Examples of such coherent vortices include Jupiter's Red Spot, tropospheric cyclones and hurricanes, stratospheric polar vortices, and oceanic Gulf Stream rings. To investigate some of the essential fluid dynamics of rotating stratified flows, we posed an idealized problem for large-scale turbulent planetary flows. We neglected the influences of spherical geometry and global-scale circulations, not because they are everywhere unimportant but because we wished to isolate the particular nonlinear dynamics of fluid advection in a uniform environment. We believe that the behavior exhibited in such idealized situations underlies many of the particular phenomena that occur in planetary flows.

A long-standing theoretical prediction (*1–3*) is that planetary turbulence evolves to have a particular form of spatial isotropy of statistical average properties. Furthermore, previous numerical assessments (*4, 5*), based on sparse and anisotropic computational grids, have appeared to confirm this prediction. We tested this prediction in a computation with a dense, fully isotropic grid (that is, there were equal numbers of points in each direction) in a spatially homogeneous, periodic domain. The solution exhibits significant anisotropy associated with the emergence of many long-lived, sparsely distributed coherent vortices that control the flow evolution. Over a very long time scale, the coherent vortices undergo successive interactions before reaching an approximate end state of the turbulent evolution, consisting of two columns, each containing vortices of common sign.

The dynamical regime called quasi-geostrophy is relevant to planetary-scale motions. It is defined by the assumption of incompressibility, small viscosity, and asymptotic approximations appropriate to a rapid rotation rate $\Omega$ and a strong, gravitationally stable ambient density stratification $d\rho/dz$. The characteristic frequencies for rotation and stratification are

$$f = 2\Omega \text{ and } N = \sqrt{-\frac{g}{\rho}\frac{d\rho}{dz}}$$

Here we restrict our attention to spatially constant $f$ and $N$. In the quasi-geostrophic regime, $f$ and $N$ are large compared with a typical eddy rotation rate, and the velocity is nearly horizontal in that the vertical component $w$ (parallel to the gravitational vector) is small compared to horizontal components $u$ and $v$. Thus, $u$ and $v$ are nearly nondivergent in $x$ and $y$ and can be represented approximately by a stream function $\psi$

$$u = -\frac{\partial\psi}{\partial y} \text{ and } v = \frac{\partial\psi}{\partial x}$$

The governing equation is

$$\frac{\partial q}{\partial t} + \frac{\partial\psi}{\partial x}\frac{\partial q}{\partial y} - \frac{\partial\psi}{\partial y}\frac{\partial q}{\partial x} = -\mathcal{D} \qquad (1)$$

where $q$ is the potential vorticity field

$$q = \frac{\partial^2\psi}{\partial x^2} + \frac{\partial^2\psi}{\partial y^2} + \frac{f^2}{N^2}\frac{\partial^2\psi}{\partial z^2} \qquad (2)$$

and $\mathcal{D}$ is a dissipation operator that represents the effects of all scales of motion smaller than those explicitly resolved in the numerical calculation.

Planetary atmospheres and oceans are typically thin fluid layers. However, the small $w$ in quasi-geostrophic theory implies small vertical length scales, and it is appropriate to use a stretched vertical coordinate, $z' = (N/f)z$, where $N/f$ is large, typically of order 100 on Earth. In this coordinate frame, $f/N$ drops out of Eq. 2, such that

$$q = \nabla^2\psi \qquad (3)$$

Consistent with our desire to test the isotropy of quasi-geostrophic solutions in the stretched coordinate frame, we choose an isotropic dissipation operator

$$\mathcal{D} = \nu\nabla^4 q \qquad (4)$$

where $\nu$ is a small hyperviscosity (*6*). Equations 1, 3, and 4 differ from the equations for two-dimensional flow only in that here $\nabla$ is three-dimensional. This led Charney (*1*) to predict that the spatially isotropic Kolmogorov theory of two-dimensional turbulent cascades (*7, 8*) should apply to quasi-geostrophic flows as well. This would imply that $\psi$ and $q$ are statistically isotropic functions of $(x, y, z')$ in the range of scales where cascades occur.

We solved Eqs. 1, 3, and 4 on a uniform grid in a periodic cube in $\mathbf{x} = (x, y, z')$ of size $2\pi L$. We pick $L$ as the largest internal deformation radius (a natural horizontal scale of response to forcing for rotating stratified fluids); typical values for the ocean and atmosphere are 50 and 1500 km, respectively. In the unstretched coordinates, the depth of the domain represents the full depth of either the ocean or the atmospheric troposphere. The initial condition in $\psi$ is a Gaussian random realization of an isotropic wave number spectrum peaked at scales intermediate between the domain and grid resolution. The posing of the problem is completely homogeneous and isotropic in initial conditions for $\psi$ and $q$, in the dissipation operator, and in the domain extent and resolution. This allows an unambiguous test of whether the solution remains isotropic.

The initial energy is

$$E = \frac{1}{2\mathcal{V}}\int |\nabla\psi|^2 d\mathbf{x} = 1$$

where $\mathcal{V}$ is the volume; this normalization defines the time scale of the evolution. The equations are discretized by finite differences and integrated by a fully implicit multigrid method (*9*). To attain high resolution, we developed an efficient parallel algorithm and implemented it on the Cray C-90 supercomputer. Solutions were calculated for a range of spatial grid resolutions, with varying hyperviscosity coefficients $\nu$, and with an alternative viscosity operator (*4, 5*) to test the robustness of our computational results. These calculations indicate that the phenomena presented here from our highest resolution $320^3$ case are representative of the quasi-geostrophic regime. We extrapolate that a solution with still higher resolution would show a richer structure on smaller spatial scales, but this is unlikely to affect the larger scale behavior described below.

J. C. McWilliams, Geophysical Turbulence Program, National Center for Atmospheric Research, Boulder, CO 80307, USA.
J. B. Weiss, Program in Atmospheric and Oceanic Sciences, Department of Astrophysical, Planetary, and Atmospheric Sciences, University of Colorado, Boulder, CO 80309, USA.
I. Yavneh, Computer Science Department, Technion, Haifa, Israel.

The initial stage of evolution is a broadening of the spectra of wave number $\mathbf{k}$. Energy is transferred preferentially toward larger scales and thus away from the smaller scales at which dissipation occurs. In contrast, potential enstrophy

$$V = \frac{1}{2\mathcal{V}}\int q^2 d\mathbf{x}$$

is transferred toward smaller scales, resulting in its dissipation (*1–3*). The effects (Fig. 1) are that $E$ decreases by only 4% over the integration but $V$ decreases by nearly two orders of magnitude. The rate of enstrophy dissipation reaches a maximum at $t \approx 1$, after several nonlinear advection (eddy recirculation) times of order $V^{-1/2}$. Thereafter, the rate of spectrum broadening diminishes, and the flow develops substantial spatial intermittency (the intense flow events occur sparsely). In particular, the kurtosis of $q$

$$K = \mathcal{V}\int q^4 d\mathbf{x} \Big/ \left(\int q^2 d\mathbf{x}\right)^2$$

grows monotonically from its initial Gaussian value and eventually reaches very large values (Fig. 1).

Figure 2 shows the wave number spectrum of $q$ averaged over all wave number directions

$$S(\kappa) = \int_\kappa |\hat{q}|^2 d\mathbf{k}$$

where $\hat{q}(\mathbf{k})$ is the three-dimensional Fourier transform of $q(\mathbf{x})$ and the integral is over wave number shells of constant wave number modulus $\kappa = |\mathbf{k}|L$. If $\hat{q}(\mathbf{k})$ is isotropic, then $S(\kappa)$ provides a complete description of the scale content of $q$. Only near the time of maximum enstrophy dissipation, $t \approx 1$ (not shown), does $S(\kappa)$ approach the $\kappa^{-1}$ inertial-range cascade form predicted by the Kolmogorov theory (*1–3, 7, 8*). Thereafter, $S(\kappa)$ has a broadband peak, is appreciably steeper than $\kappa^{-1}$ in the inertial range, and has a steep decay in the dissipation range at very large $\kappa$. Its evolution shows slow movement of its peak toward smaller $\kappa$ and steepening in the inertial and dissipation ranges.

To test for anisotropy, we constructed the measure

$$A(\kappa) = \frac{3S_{z'}(\kappa)}{S_x(\kappa) + S_y(\kappa) + S_{z'}(\kappa)} \qquad (5)$$

on the basis of the directionally weighted spectra

$$S_\eta(\kappa) = \int_\kappa \left(\frac{\kappa_\eta}{\kappa}\right)^2 |\hat{q}|^2 d\mathbf{k}$$

with $\eta = x,y,z'$. The $S_\eta$ provide a directionally weighted decomposition of $S$, that is, $\Sigma_\eta S_\eta = S$. If $q$ is isotropic, then $S_\eta = \frac{1}{3}S$ and $A = 1$. Our solution shows significant departures from isotropy (Fig. 3): At intermediate and large $\kappa$, $A > 1$ in two distinct wave number bands. The former is in the inertial range, contradicting the Charney isotropy prediction, and the latter is in the dissipation range. The degree of inertial-range anisotropy grows systematically after the time of maximum dissipation rate. In the vicinity of the spectrum peak (Fig. 2), $A$ indicates approximate isotropy. At smaller values of $\kappa$, there is even an indication of an opposite sense of anisotropy, but here the sampling error is appreciable because there are few wave numbers to average over.

The spectrum evolution and increase in intermittency and anisotropy are associated with the emergence of coherent vortices, seen as isolated concentrations of $q$ (Fig. 4). The effects of vortices are absent in the Kolmogorov theory; we believe that their occurrence is the reason the isotropy prediction fails. Although previous numerical tests (*4, 5*) did show vortices, their vertical grid was too sparse to detect the inertial-range anisotropy.

The typical vortex shape near the time of emergence (Fig. 4A) is a roughly spherical blob of $q(x,y,z')$, with monotonic decay from the central extremum to nearly zero at the edge of the vortex. The velocity field of the vortex is mostly azimuthal and axisymmetric about a vertical axis. Each such vortex is, by itself, a stable, stationary state of the inviscid dynamics that results from the organizing processes of horizontal axisymmetrization and vertical alignment (*5, 10–12*).

The vortices move by mutual advection in an essentially conservative fashion, except during close approaches when dissipative interactions occur. The most important of these occur between like-sign vortices: a merger (*13*), where most of the core material of two vortices becomes intertwined to form a single, larger vortex, and vertical alignment (*5*) of vortices that can remain distinct. With time, these processes reduce the vortex population and result in larger, vertically grouped vortices (Fig. 4, B and C).

Over a very long time scale, comparable to that spanned by Fig. 4, the chaotic mutual advection leads to a succession of vortex mergers and alignments. The vortex groups become fewer and, in a finite domain, evolve into a configuration consisting of two vertical columns. Each column contains many vortex cores, with one containing only positive cores and the other only negative. In this configuration, the only subsequent nonconservative evolution is very slow diffusion, with correspondingly slow changes in $S(\kappa)$. Figure 4D is approaching this state, although not all the vortex interactions have as yet occurred. In some coarse-grained sense, this end state

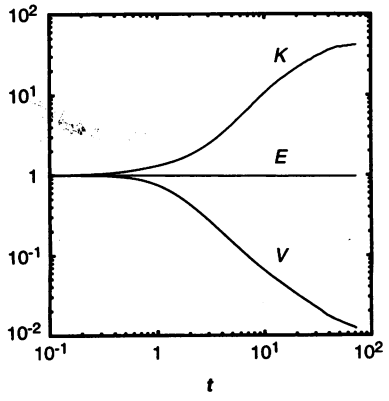


**Fig. 1.** Time series of the energy $E$, potential enstrophy $V$, and kurtosis $K$. All quantities are normalized by their initial values. These show the cascade tendencies of energy conservation, enstrophy dissipation, and intermittency growth.

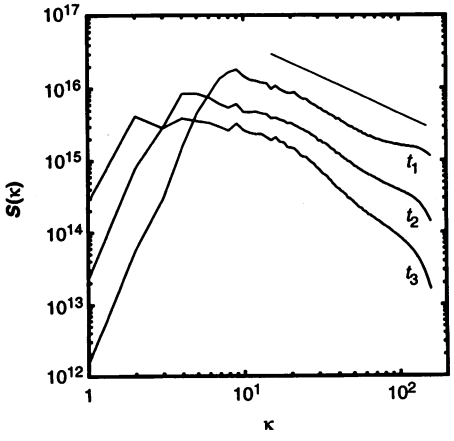


**Fig. 2.** Wave number spectra of potential vorticity, $S(\kappa)$, at $t_1 = 2.2$, $t_2 = 5.0$, and $t_3 = 10.0$. The interval from the spectrum peak to $\kappa \approx 100$ is the "inertial range," and the "dissipation range" has $\kappa > 100$. The reference line is proportional to $\kappa^{-1}$, the classical inertial-range prediction (*1–3, 7, 8*).

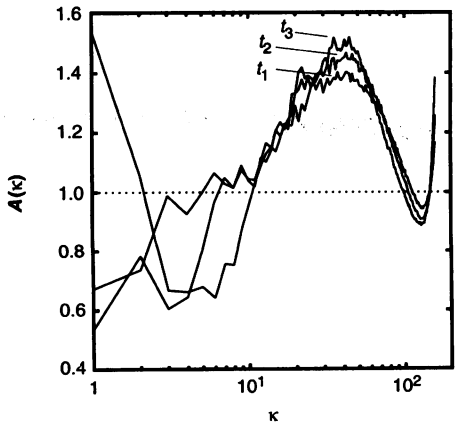


**Fig. 3.** Spectrum anisotropy $A(\kappa)$ (Eq. 5) at the same times as in Fig. 2. A value of $A(\kappa) \neq 1$ indicates an anisotropic potential vorticity distribution at wave number $\kappa$.

resembles vertically uniform columns of potential vorticity, which would have accompanying depth-independent (barotropic) motion. Such an outcome has been seen in simulations with very coarse vertical resolution (*14*). However, the actual end state is significantly different from barotropic motion and, because there is no inviscid mechanism for vertical homogenization of the potential vorticity, will remain so.

Coherent vortices occur abundantly in nature, and the particular examples mentioned in the introduction are known to contribute significantly to the dynamical balances of the global circulations. The turbulent vortex dynamics shown here must, in nature, compete with other influences such as global circulations, small-scale forcing, inhomogeneities in $N$ and $f$, and anisotropic domains. Nevertheless, our idealized model exhibits the fundamental phenomena of vortex emergence and evolution and allows us to study their roles in the statistical dynamics of planetary turbulence.

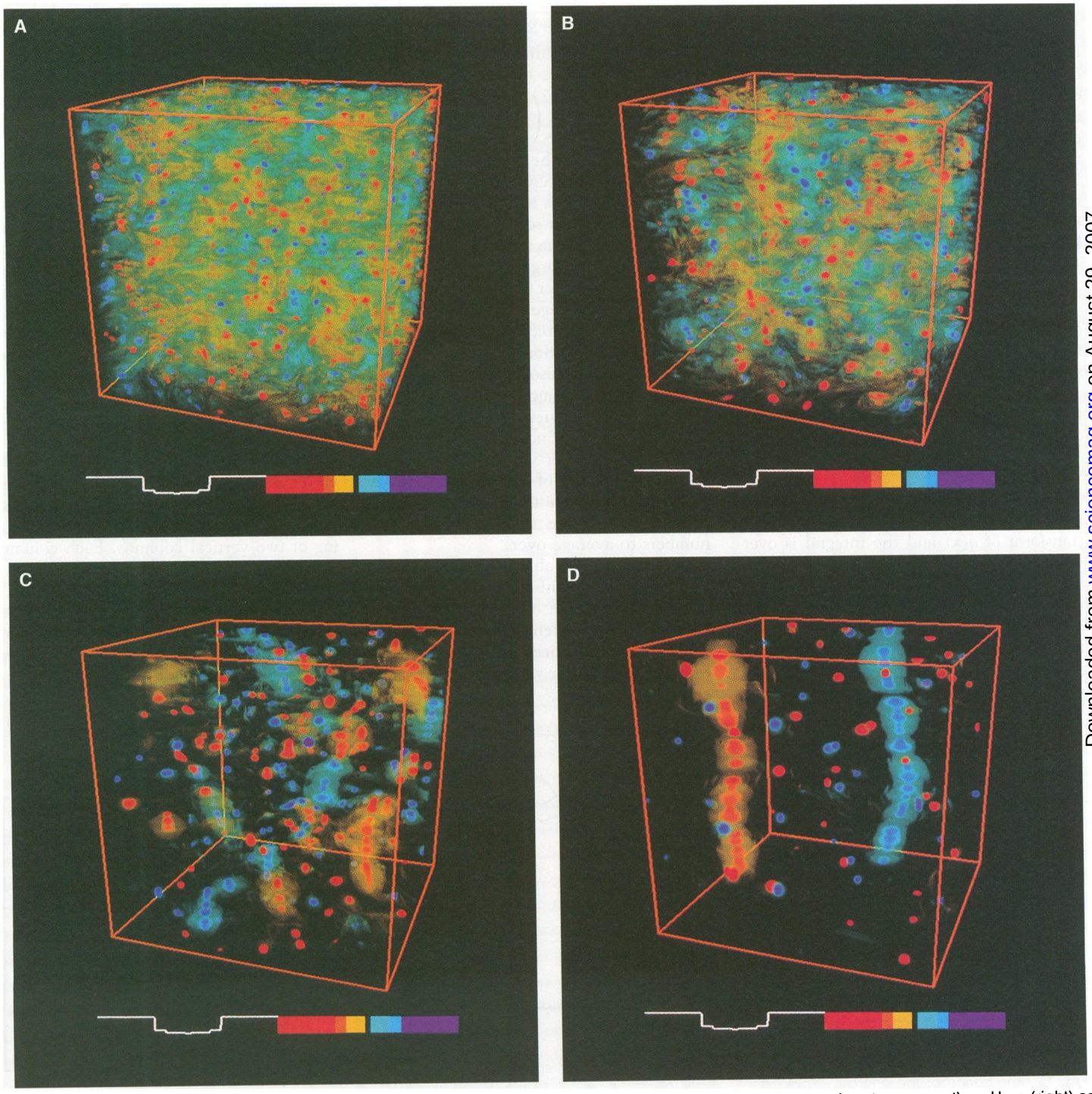


**Fig. 4.** Potential vorticity $q(x,y,z')$ at (**A**) $t$ = 5.0, (**B**) $t$ = 10.0, (**C**) $t$ = 25.6, and (**D**) $t$ = 72.1. The $z'$ axis is up. The data are displayed by a volume-rendering technique: Each grid value is assigned a color and degree of transparency affecting light rays that pass through the volume to the viewer. The curves beneath the images show the transparency (left) (larger values are less transparent) and hue (right) as a function of $q$, centered about $q$ = 0. Thus, for example, a large positive $q$ is purple and opaque, whereas a smallish negative $q$ is yellow and fairly transparent. Very small $|q|$ is completely transparent, hence, invisible.

## REFERENCES AND NOTES

1. J. G. Charney, *J. Atmos. Sci.* **28**, 1087 (1971).
2. P. B. Rhines, *Annu. Rev. Fluid Mech.* **11**, 401 (1979).
3. J. Herring, *J. Atmos. Sci.* **37**, 969 (1980).
4. L. B. Hua and D. B. Haidvogel, *ibid.* **43**, 2923 (1986).
5. J. C. McWilliams, *J. Fluid Mech.* **198**, 199 (1989).
6. R. Sadourny and C. Basdevant, *C. R. Acad. Sci.* **39**, 2138 (1981).
7. A. N. Kolmogorov, *J. Fluid Mech.* **13**, 82 (1962).
8. R. H. Kraichnan, *Phys. Fluids* **10**, 1417 (1967).
9. I. Yavneh and J. C. McWilliams, in preparation.
10. M. V. Melander, J. C. McWilliams, N. J. Zabusky, *J. Fluid Mech.* **178**, 137 (1987).
11. L. Polvani, *ibid.* **225**, 241 (1991).
12. D. Dritschel and R. Saravanan, *Q. J. R. Meteorol. Soc.*, in press.
13. M. V. Melander, N. J. Zabusky, J. C. McWilliams, *J. Fluid Mech.* **195**, 303 (1988).
14. P. B. Rhines, in *The Sea*, E. D. Goldberg, I. N. McCave, J. J. O'Brien, J. H. Steele, Eds. (Wiley, New York, 1977), vol. 6, pp. 189–318.



15. Sponsored by the National Science Foundation through the National Center for Atmospheric Research, the Pittsburgh Supercomputing Center, and the United States–Israel Bilateral Science Foundation. We thank L. Hua for helping us refine our measure of anisotropy and N. Norton for her valuable computational assistance.

13 December 1993; accepted 7 March 1994


# Thousandfold Change in Resistivity in Magnetoresistive La-Ca-Mn-O Films


S. Jin, T. H. Tiefel, M. McCormack, R. A. Fastnacht, R. Ramesh, L. H. Chen



**A negative isotropic magnetoresistance effect more than three orders of magnitude larger than the typical giant magnetoresistance of some superlattice films has been observed in thin oxide films of perovskite-like $La_{0.67}Ca_{0.33}MnO_x$. Epitaxial films that are grown on $LaAlO_3$ substrates by laser ablation and suitably heat treated exhibit magnetoresistance values as high as 127,000 percent near 77 kelvin and ~1300 percent near room temperature. Such a phenomenon could be useful for various magnetic and electric device applications if the observed effects of material processing are optimized. Possible mechanisms for the observed effect are discussed.**


Giant magnetoresistance (GMR) caused by spin-dependent scattering in metallic multilayers (*1–5*), heterogeneous alloy films (*6*, *7*), and spinodally decomposed alloys (*8*) has attracted considerable attention in recent years for fundamental physics as well as device applications such as magnetic recording heads (*9*). The GMR effect is characterized not only by its large magnetoresistance (MR) ratio, typically −5 to −50% as compared to ~+3% for the 80% Ni–20% Fe type permalloy, but also by its negative value and isotropic (independent of field orientation) nature (*7*). The MR ratio is defined here as $\Delta R/R_H = (R_H - R_0)/R_H$, where $R_0$ is the resistance at a magnetic field of $H = 0$ and $R_H$ is $R$ at $H = 6$ T.

The largest reported value of $\Delta R/R_H$ for metallic materials was ~−150% for Fe-Cr multilayer films measured at 4.2 K (*4*). More recently, a large MR effect was also reported for naturally layer-structured materials, such as the intermetallic compound Sm-Mn-Ge (*10*), and the magnetic oxide films of perovskite-like Nd-Pb-Mn-O (*11*), La-Ba-Mn-O (*12*), and La-Ca-Mn-O (*13*). The La-Ba-Mn-O films gave a $\Delta R/R_H$ value of as large as −150% at room temperature, whereas the La-Ca-Mn-O films gave a value of ~−110% at ~220 K but ~0% at room temperature. The perovskite-like crystal structure of these compounds exhibit ferromagnetic ordering in the crystallographic *ab* planes (Mn-O layers), separated by nonmagnetic La(Ca)-O layers, and antiferromagnetic ordering along the *c* axis (*14*). The mixed $Mn^{3+}$-$Mn^{4+}$ valence state in these compounds is responsible for the occurrence of both ferromagnetism and metallic conductivity (*15*, *16*).

We prepared epitaxial thin films of La-Ca-Mn-O, 1000 to 2000 Å thick, on (100) $LaAlO_3$ substrates by pulsed laser deposition. The target, with a nominal composition of $La_{0.67}Ca_{0.33}MnO_x$, was made by the mixing of high-purity component oxides or carbonates and repeated grinding and sintering at ~1000° to 1300°C for 16 hours in oxygen. The substrate temperature was maintained at 600° to 700°C during deposition. The deposition was carried out under 100 mtorr partial $O_2$ atmosphere.

The MR of the films, typically ~1000 Å thick, ~2 mm wide, and ~4 mm long, was measured by the four-point technique (at a constant current) in a superconducting magnet with the maximum applied field of 6 T. The direction of the field was the same as that of the current. Some of the samples were measured with the field perpendicular to the current direction, which showed the MR to have no obvious dependence on field orientation (that is, it is nearly isotropic) if the demagnetizing factor is taken into consideration. We obtained M-*H* loops with a vibrating sample magnetometer in a field of up to 1 T.

The chemical composition of the deposited films, as determined by scanning electron microscope microanalysis and Rutherford backscattering, was found to be essentially identical to that of the bulk target material used for the laser ablation deposition. The results of x-ray diffraction, rocking angle analysis, and transmission electron microscopy indicate that the films have a cubic crystal structure (lattice parameter $a \approx 3.89$ Å) and grow epitaxially on the (100) $LaAlO_3$ substrate ($a \approx 3.79$ Å).

The temperature dependence of the MR ratio for the as-deposited sample (substrate temperature, ~640°C) shows a high peak MR ratio of −460% near 100 K (Fig. 1). Subsequent annealing heat treatment moved the peak in the as-deposited film to a higher temperature with a narrower distribution. Processing at 700°C for 30 min in an $O_2$ atmosphere raised the peak temperature to ~200 K and gave a $\Delta R/R$ value of about −1400%. Processing optimizations have led to a further improved MR in excess of ~−100,000% near 77 K.

It is not clearly understood why the $\Delta R/R$ value and the peak temperature in the deposited films change with the heat-treatment temperature and time. Several possibilities include the effect of heat treatment on oxygen stoichiometry, epitaxy, defect density, chemical homogenization, and substrate-film chemical reactions.

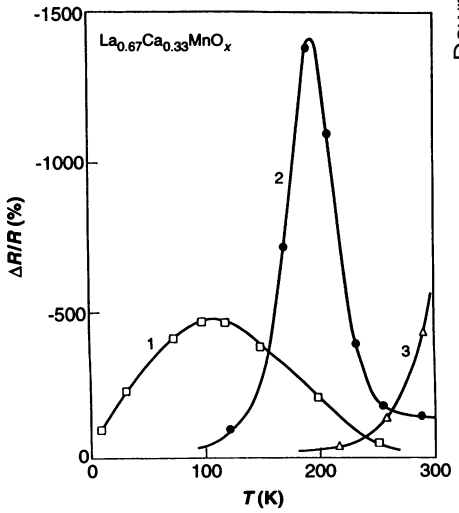


**Fig. 1.** Three MR ratio ($\Delta R/R_H$) versus temperature curves for the La-Ca-Mn-O films. Curve 1, as deposited; curve 2, heated to 700°C for 0.5 hour in an $O_2$ atmosphere; and curve 3, heated to 900°C for 3 hours in $O_2$.


S. Jin, T. H. Tiefel, M. McCormack, R. A. Fastnacht, AT&T Bell Laboratories, Murray Hill, NJ 07974, USA.
R. Ramesh, Bellcore, Red Bank, NJ 07701, USA.
L. H. Chen, Kaohsiung Polytechnique Institute, Ta-Hsu Hsiang, Taiwan.